

# SERS Quantification of Galunisertib Delivery in Colorectal Cancer Cells by Plasmonic-Assisted Diatomite Nanoparticles

Stefano Managò, Chiara Tramontano, Donatella Delle Cave, Giovanna Chianese, Gianluigi Zito, Luca De Stefano, Monica Terracciano, Enza Lonardo,\* Anna Chiara De Luca,\* and Ilaria Rea\*

The small molecule Galunisertib (LY2157299, LY) shows multiple anticancer activities blocking the transforming growth factor- $\beta$ 1 receptor, responsible for the epithelial-to-mesenchymal transition (EMT) by which colorectal cancer (CRC) cells acquire migratory and metastatic capacities. However, frequent dosing of LY can produce highly toxic metabolites. Alternative strategies to reduce drug side effects can rely on nanoscale drug delivery systems that have led to a medical revolution in the treatment of cancer, improving drug efficacy and lowering drug toxicity. Here, a hybrid nanosystem (DNP-AuNPs-LY@Gel) made of a porous diatomite nanoparticle decorated with plasmonic gold nanoparticles, in which LY is retained by a gelatin shell, is proposed. The multifunctional capability of the nanosystem is demonstrated by investigating the efficient LY delivery, the enhanced EMT reversion in CRCs and the intracellular quantification of drug release with a sub-femtogram resolution by surface-enhanced Raman spectroscopy (SERS). The LY release trigger is the pH sensitivity of the gelatin shell to the CRC acidic microenvironment. The drug release is real-time monitored at single-cell level by analyzing the SERS signals of LY in CRC cells. The higher efficiency of LY delivered by the DNP-AuNPs-LY@Gel complex paves the way to an alternative strategy for lowering drug dosing and consequent side effects.

therapies for CRC treatment, like systemic chemotherapy and immunotherapy, are expensive and invasive since they fail to target cancer cells selectively, causing severe toxicity on normal tissues besides side effects.<sup>[2-5]</sup> The epithelial-to-mesenchymal transition (EMT) is a dynamic multistep process involved in several physiological and pathological conditions, including cancer.<sup>[6]</sup> Notably, EMT in CRC is associated with an invasive, metastatic, and chemoresistant phenotype.<sup>[7]</sup> In contrast, the mesenchymal-to-epithelial transition (MET), is the reverse program of EMT in metastases and is characterized by the upregulation of epithelial adhesive proteins such as E-CADHERIN, and downregulation of mesenchymal proteins, such as SNAIL-1 and TWIST-1. Slowing EMT or even reversing the process in metastases inducing a MET program not only is a powerful therapeutic approach alone, but can also assist in increasing the efficacy of other anticancer treatments. Among the molecular pathways promoting tumorigenesis in CRC, the

transforming growth factor- $\beta$  (TGF- $\beta$ ) is described as a crucial factor in EMT induction.<sup>[8]</sup> Fighting the CRC with the TGF- $\beta$  receptor I-specific inhibitor Galunisertib (LY2157299, LY) has been proposed as a powerful strategy to reduce tumor growth and the risk of relapse.<sup>[8]</sup> However, LY is cleared predominantly by cytochrome P450 3A4 (CYP3A4) oxidative metabolism in the

## 1. Introduction

According to GLOBOCAN 2020 data, colorectal cancer (CRC) is the fourth most diagnosed cancer in the world. Despite the advances in diagnosis and surgical procedures, 20% of CRC patients manifest metastasis at the time of diagnosis, which of course affects the patient survival rate.<sup>[1]</sup> Most of the conventional

Dr. S. Managò, Dr. A. C. De Luca  
National Research Council  
Institute of Biochemistry and Cell Biology  
Naples 80131, Italy  
E-mail: annachiara.deluca@cnr.it

 The ORCID identification number(s) for the author(s) of this article can be found under <https://doi.org/10.1002/smll.202101711>.

© 2021 The Authors. Small published by Wiley-VCH GmbH. This is an open access article under the terms of the Creative Commons Attribution License, which permits use, distribution and reproduction in any medium, provided the original work is properly cited.

DOI: 10.1002/smll.202101711

C. Tramontano, G. Chianese, Dr. G. Zito, Dr. L. De Stefano, Dr. I. Rea  
National Research Council  
Institute of Applied Sciences and Intelligent Systems  
Unit of Naples  
Naples 80131, Italy  
E-mail: ilaria.rea@cnr.it

C. Tramontano, Dr. M. Terracciano  
University of Naples Federico II  
Department of Pharmacy  
Naples 80131, Italy

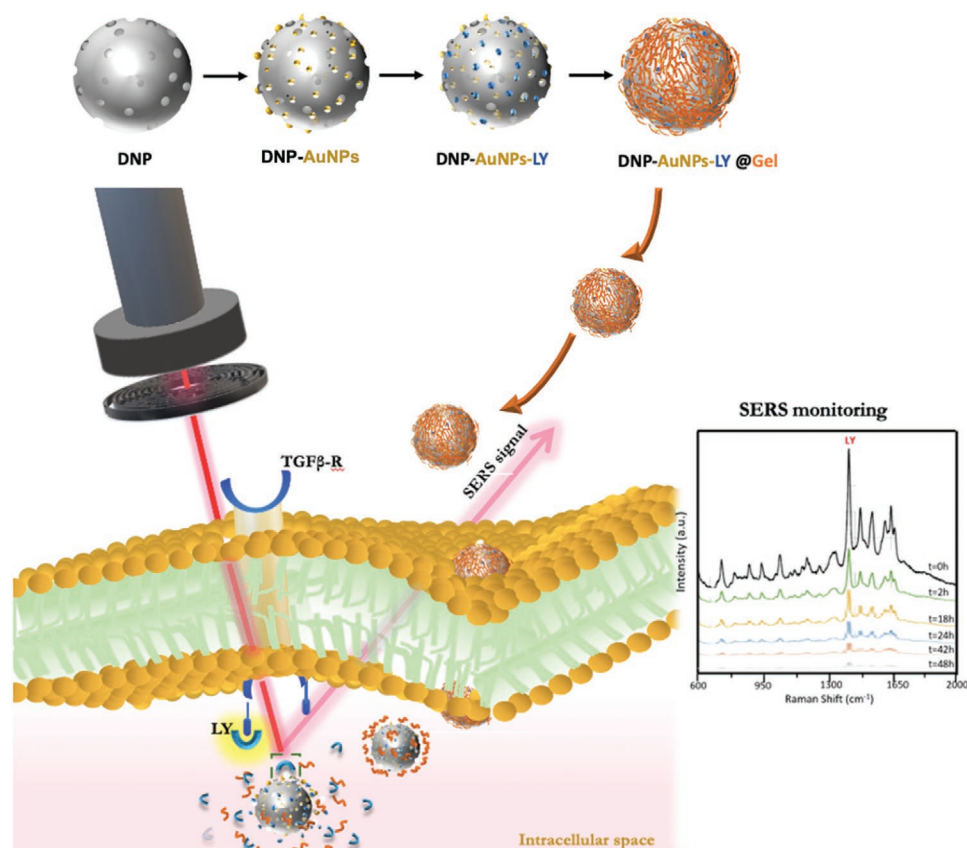
Dr. D. Delle Cave, Dr. E. Lonardo  
National Research Council  
Institute of Genetics and Biophysics  
Naples 80131, Italy  
E-mail: enza.lonardo@igb.cnr.it

liver, which leads to the formation of diverse toxic metabolites circulating in the plasma.<sup>[9]</sup> Thus, increasing the efficacy of LY delivery to CRC cells, promoting good results with reduced dosing, is the first crucial step to tackle side effects.

In this context, nanotechnology can play a key role. Indeed, biocompatible nanoparticles (NPs) able to carry therapeutic molecules inside cancer cells represent an excellent strategy to increase drug efficacy. In particular, the surface functionalization of NPs can enhance therapy selectivity and site-specific delivery of the drug. Targeted therapy can limit the mutual interactions between the drug and normal tissues, thus reducing systemic toxicity. In addition, NPs may overcome poor oral bioavailability of drugs and their instability in circulation. Several types of NPs, such as organic, inorganic, and biological NPs, as well as their combinations, have been explored in biomedicine.<sup>[10–19]</sup> We focused our attention on inorganic diatomite NPs (DNPs) obtained from diatoms and made of a natural biosilica. Indeed, DNPs have been explored as drug delivery systems thanks to their advantageous properties, including high surface-to-volume ratio, long half-life, and chemical stability in physiological conditions.<sup>[20–22]</sup> In addition, diatom's amorphous silica is approved by the Food and Drug Administration (FDA), Generally Recognized as Safe for food and pharmaceutical production (GRAS, 21 CFR 182.90), and classified in the 3<sup>rd</sup> group of “Not classifiable as to its carcinogenicity to humans” by the International Agency for Research on Cancer (IARC).<sup>[23]</sup> DNPs can be easily prepared

in the size range of 100–400 nm and possess nanopores able to load a wide range of therapeutic compounds, including aptamers, chemotherapeutic agents, and small molecules.<sup>[23]</sup> The easy-to-tune surface of DNPs offer the opportunity to perform several surface functionalization strategies to enhance their biocompatibility, intracellular uptake, and improve drug loading and delivery efficiency.<sup>[24–27]</sup> In a previous study, we have already demonstrated the cell internalization of small-interfering RNA (siRNA)-modified DNPs via endocytic uptake. The DNPs penetrate cells within 18 h without causing toxicity and they are embedded in a lipid environment in the cytoplasmic region of cancer cells. Therefore, we consider DNPs as excellent candidates to promote enhanced LY delivery in CRC cells.<sup>[28]</sup>

To this end, in this work, we moved a crucial step forward devising a hybrid nanosystem constituted by a DNP decorated with AuNPs and capped with a gelatin (Gel) layer (**Scheme 1**) for LY delivery in CRC cells and concurrent quantification of LY release at the single-cell level with attogram-scale resolution via SERS imaging. The biocompatibility of the DNP-AuNPs complex has been preliminary demonstrated in HeLa cells during previous investigations.<sup>[29]</sup> The outer shell of gelatin is introduced to induce the sustained release of LY via degradation of the polymer chains. Gelatin-functionalized nanocarriers have already been employed for the treatment of CRC, where matrix metalloproteinase-2 (MMP-2) is overexpressed and can degrade the gelatin shell.<sup>[30]</sup> The realized nanosystem, denoted as



**Scheme 1.** Schematic diagram of DNP-AuNPs-LY@Gel synthesis and internalization in CRC cell. The acidic tumor microenvironment induces the degradation of the gelatin layer covering the DNP-AuNPs-LY@Gel nanosystem and the release of LY in the cell. The amount of the released drug can be quantified through time-dependent SERS monitoring.

DNP-AuNPs-LY@Gel, is a multifunctional platform serving as both a pH-triggered drug delivery system and SERS-nanosensor for intracellular release of LY. The release of LY from the nanocomplex is both time and pH-dependent. At physiological pH (7.4) the gelatin layer is folded tightly and the drug is retained in the nanosystem. In contrast, due to the sufficient extension of gelatin chains and degradation of some gelatin molecules in the acidic environment, the release of LY is promoted at pH 5.5. This pH-dependent drug delivery behavior is useful to trigger the release of LY in CRC, where the accumulation of lactic acid in the close external microenvironment and the overexpression of MMP-2 make the physiological pH acidic.<sup>[31]</sup> The monitoring of the nanosystem internalization and LY release quantification is made possible by the presence of suitable AuNPs on the DNP providing a highly sensitive SERS readout of LY with non-invasive laser illumination exciting their plasmonic resonance. Indeed, the intracellular release of LY to CRC is measured by SERS as a function of the incubation time up to 48 h and relatively quantified to provide the LY sensogram evolution with an unprecedented resolution of  $7.5 \times 10^{-18}$  g. The quantification of the intracellular drug release from NP-based systems is essential for correlating the amount of internalized drug with the therapeutic effect induced in the cell. At present, many drug release monitoring systems are limited to qualitative determination or they lack precise quantification due to imaging sensitivity and resolution. The urgency for monitoring the drug release in real-time can be satisfied by loading fluorescence payloads in NPs and quantifying the intracellular release by fluorescence measurements.<sup>[32]</sup> This work describes an alternative, accurate, and label-free method based on SERS analysis for the intracellular quantification of LY release. We also demonstrate that the release of LY from the DNP-AuNPs-LY@Gel complex inside the CRC cells inhibits their proliferation and induces the reversion to a normal phenotype by MET with greater efficiency compared to the free drug.

## 2. Results and Discussion

### 2.1. DNP-AuNPs-LY@Gel Nanosystem Preparation and Characterization

The DNP-AuNPs-LY@Gel nanosystem was prepared following the fabrication procedure reported in Scheme 1. Aminosilanized DNP (reported in the text as “DNP”) resulted in a mean size of  $400 \pm 50$  nm and a surface  $\zeta$ -potential of  $20 \pm 5$  mV; the positive surface charge was related to the presence of amino groups on the surface of the DNP. At this stage, the colloidal suspension of DNPs in de-ionized water appeared colorless. To decorate the surface of the DNP with metallic NPs, DNPs were dispersed in a chloroauric acid solution. The amine groups on the surface of the DNP allowed the electrostatic interaction between DNP-NH<sup>3+</sup> and AuCl<sup>4-</sup> gold precursor ions. The NaBH<sub>4</sub> solution was used to reduce the gold precursor ions in gold NPs (AuNPs). The resulted hybrid system DNP-AuNPs had a mean size comparable to which of the bare DNP within the error ( $400 \pm 50$  nm). Its  $\zeta$ -potential decreased to  $-15 \pm 10$  mV due to the presence of the carboxyl groups of dicarboxylic PEG embedding the AuNPs and used as a stabilizing agent in the

AuNPs synthesis.<sup>[29,33]</sup> The presence of the AuNPs on the surface of the DNP was confirmed by the color change of the suspension that turned from transparent to light purple. The porosity structure of DNP-AuNPs and their surface area of about  $6 \text{ m}^2 \text{ g}^{-1}$  (measured by gas porosimetry, data not shown here) was exploited to realize a drug delivery system with efficient drug loading and release capacity.<sup>[29]</sup> In this work, the small molecule LY used in clinical trials for the treatment of different types of cancer including CRC was loaded in the DNP-AuNPs nanocomplex. The loading of LY in the inner and outer surface of the DNP-AuNPs nanocomplex was performed in an acidic solution to promote the electrostatic interactions between the protonated isoform of the drug and dicarboxylic PEG molecules surrounding the DNP-AuNPs complex. Specifically, the elaborate chemical structure of LY can be protonated on various functional groups according to the multiple isoforms generated under different pH conditions. In this study, the acidic drug loading solution promoted the protonation of the quinoline-carboxamide group of LY and its attraction to the negative charges of the surface AuNPs. In addition, the chemisorption interactions (N-Au type) between the drug and AuNPs supported the loading of LY in the complex DNP-AuNPs.<sup>[34,35]</sup> The nanosystem loaded with LY (DNP-AuNPs-LY) was finally capped with a layer of gelatin crosslinked by carbodiimide chemistry to prevent the burst release of the drug in aqueous solution. The DNPs-AuNPs-LY system was dispersed in an acidic solution of gelatin at pH 3.5 to preserve the electrostatic interactions between LY and the nanosystem. Finally, the gelatin adsorbed on the surface of the DNP-AuNPs-LY was crosslinked and the DNP-AuNPs-LY@Gel final complex still purple in color was characterized. The characterizations of DNPs revealed an increment of the mean size to  $450 \pm 50$  nm and a surface  $\zeta$ -potential of  $-7 \pm 8$  nm. The change of the  $\zeta$ -potential to an almost neutral value ( $-7 \pm 8$  mV) was ascribed to the crosslinking phenomena occurring on the surface of the gelatin layer that reserved both carboxyl and amino groups, providing the nanosystem with a neutral surface. (Figure 1a,b).

The morphological changes of the nanocomplex were highlighted by transmission electron microscopy (TEM) analysis (Figure 1c). The DNP 400 nm in size was characterized by an irregular shape and a porous morphology; pores with a size range between 15 and 35 nm were observed in TEM investigations. The pore size was calculated using a free-open-source image processing package (Image J). Previous studies demonstrated that the irregular shape of the DNP did not induce cellular toxicity.<sup>[20,28]</sup> The in situ synthesis of AuNPs promoted the growth of a dense coverage of AuNPs on the surface of the DNP. According to TEM analysis, the mean size of AuNPs on the biosilica surface was about 25 nm. The DNP-AuNPs-LY@Gel nanosystem showed a morphology similar to that of the DNP before the drug loading and gelatin capping, revealing that the exposure to the chemical reagents used in the functionalization procedure (i.e., acetone, acidic solutions) did not alter the morphology of the nanosystem. The presence of the gelatin layer, visible as a thin and clear ring around the DNPs in TEM investigations, was further confirmed by UV-Vis analysis. Figure 1d reports the absorbance spectra of bare DNPs, DNPs-AuNPs, and DNPs-AuNPs-LY@Gel suspended in de-ionized water. The suspension of DNPs did not show absorption

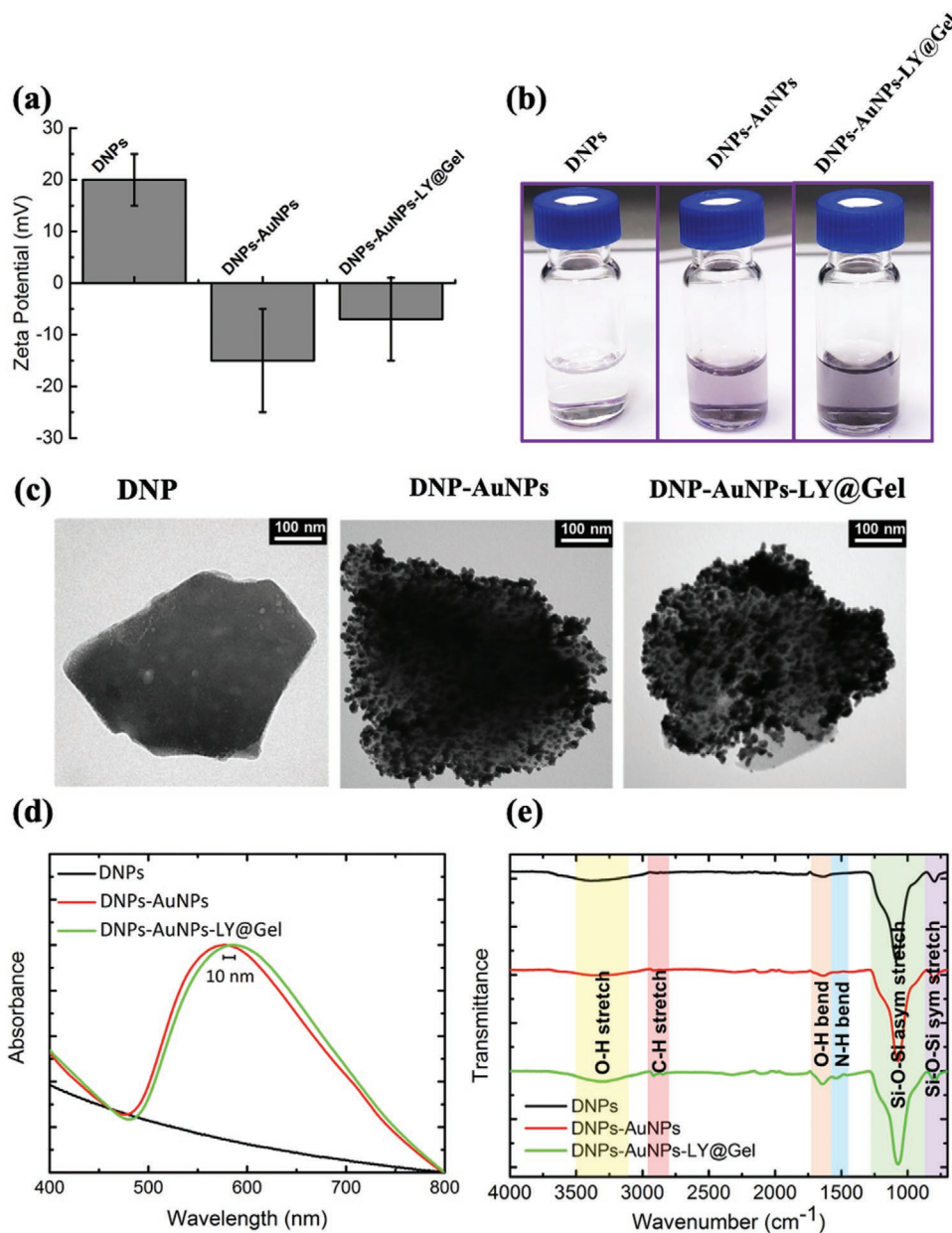


**Figure 1.** a)  $\zeta$ -potential of a suspension of bare DNPs, DNPs-AuNPs, and DNPs-AuNPs-LY@Gel reported as mean ( $n = 5$ )  $\pm$  SD. b) Images of vials containing a suspension of bare DNPs, DNPs-AuNPs, and DNPs-AuNPs-LY@Gel in de-ionized water. c) TEM images of the bare DNP, DNP-AuNPs, and DNP-AuNPs-LY@Gel complex. d) UV-Vis spectra of a suspension of bare DNPs, DNP<sub>5</sub>-AuNPs, and DNPs-AuNPs-LY@Gel in de-ionized water. e) FTIR spectra of DNPs, DNPs-AuNPs, and DNPs-AuNPs-LY@Gel. The peaks corresponding to the predominant chemical groups present in the samples are highlighted.

peaks in the visible range under investigation (black curve in Figure 1d). The Localized Surface Plasmon Resonance (LSPR) of AuNPs on the biosilica surface was observed at 576 nm through absorbance spectroscopy (red curve in Figure 1d). The presence of LY loaded in the nanocomplex could not be detected through changes in the LSPR of the DNPs-AuNPs-LY suspension, due to the small size of LY (data not shown here). Conversely, the gelatin capping in the DNP-AuNPs-LY@Gel complex caused a 10 nm red-shift of the LSPR due to the increase of the effective refractive index in the NP surroundings.<sup>[36]</sup> Figure 1e shows the FTIR spectra of the DNPs (black curve), DNPs-AuNPs

(red curve), and DNPs-AuNPs-LY@Gel (green curve) suspension. FTIR spectra of samples were characterized by two peaks at 1100 and 800  $\text{cm}^{-1}$  related to the asymmetric and symmetric stretching modes of siloxane (Si-O-Si), respectively;<sup>[37]</sup> the features at 3400 and 1640  $\text{cm}^{-1}$  were due to the O-H stretching and O-H bending of water physically absorbed on the silica surface.<sup>[38]</sup> The presence of the gelatin layer on the surface of the DNPs-AuNPs-LY@Gel dispersion was demonstrated by the peaks at 1530 and 1450  $\text{cm}^{-1}$  related to N-H bending (Amine II), and the features at 2910 and 2840  $\text{cm}^{-1}$  due to the C-H stretching vibrations.<sup>[39]</sup>

## 2.2. Evaluation of the Loading and Release Capacity of DNP-AuNPs-LY@Gel

For the design of a sustained-release system, gelatin was selected as a capping element due to its advantageous features, including biodegradability, biocompatibility, and pH-responsive behavior. After the LY loading and gelatin capping, the DNP-AuNPs-LY@Gel nanosystem was immersed in an acidic solution of PBS and gently shaken for 48 h. The amount of drug-loaded in the nanocomplex (i.e., the loading capacity) was determined by analyzing the release solution by Reversed Phase-High Performance Liquid Chromatography (RP-HPLC) after 48 h. The loading capacity of LY in the nanosystem resulted to be  $20 \pm 4 \mu\text{g mg}^{-1}$  of the DNP-AuNPs-LY@Gel complex. To investigate the release behavior of the nanosystem, we performed in vitro release tests under physiological (7.4) and more acidic (5.5) pH conditions, mimicking the tumor micro-environment. The “Warburg effect” is a well-accepted theory according to which cancer cells produce energy from glucose essentially through the glycolytic pathway. This effect leads to the production of huge amounts of lactate that decreases the tumor microenvironment pH value.<sup>[40]</sup> The DNP-AuNPs-LY@Gel nanosystem exhibited a pH and time-dependent release behavior of LY in phosphate-buffered saline (PBS) at 37 °C. As shown in **Figure 2**, the cumulative release of LY increased significantly with decreasing solution pH due to the gelatin matrix embedding the NPs. When the DNP-AuNPs-LY@Gel was dispersed in PBS solution at pH 7.4, the amount of LY released to the medium was less than 10% of the total LY loaded in the nanocomplex. This phenomenon can be explained considering that the attractive forces between the opposite charges of each gelatin molecule promoted the formation of intermolecular hydrogen bonding between the gelatin molecules at physiological pH value.<sup>[41]</sup> In the PBS solution 7.4, the gelatin matrix was folded tightly and almost all the drug was retained in the nanosystem within 48 h of incubation in the release solution. Since the electrostatic attraction between the gelatin molecules decreases in a more acidic environment, when the DNP-AuNPs-LY@Gel complex was dispersed in an acidic solution the relaxation of the gelatin chains promoted the release of LY to the medium in a time-dependent manner (sigmoidal release profile). The release of LY from DNP-AuNPs-LY@Gel started after 10 h and gradually increased due to the extension of the gelatin chains that were disrupted after 48 h of incubation in the acidic solution. When the gelatin matrix was completely dissolved, 100% of the LY was released into the medium. To highlight the advantages of our system, we also carried out in vitro release tests of the DNP-AuNPs-LY complex in both acidic and physiological microenvironments (Figure S1, Supporting Information). The uncapped nanosystem exhibited a typical burst release profile, completely uncontrolled and without any sensitivity to pH value of the release solution. Indeed, the release profiles of the DNP-AuNPs-LY complex in PBS solutions 5.5 and 7.4 were comparable within the errors. Therefore, the gelatin coating in the DNP-AuNPs-LY@Gel complex not only delayed the release of LY up to 48 h, but it also prevented the uncontrolled burst release typically attributed to porous NP-based systems.<sup>[42]</sup> Moreover, the choice of the gelatin for the surface coating was based on the pathophysiological

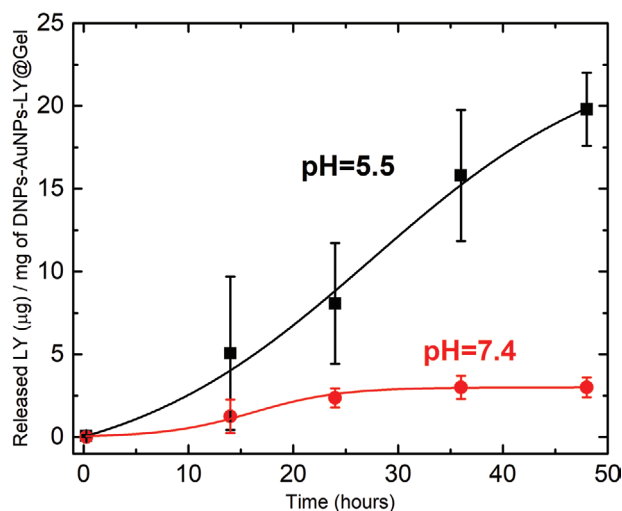


**Figure 2.** Drug release behavior of the DNP-AuNPs-LY@Gel complex in PBS solution at different pH values. The DNP-AuNPs-LY@Gel nanosystem showed a sigmoidal release behavior due to the presence of the gelatin layer embedding the nanosystem. The release of LY was strongly affected by the pH value of the PBS solution. The release was expressed as the mass of LY ( $\mu\text{g}$ ) released from 1 mg of DNP-AuNPs-LY@Gel.

properties of cancer and offered the opportunity of achieving stimuli-responsive drug release at tumor sites. In the cell, the upregulation of proteolytic enzymes degrading the gelatin chains, such as the MMP-2, can trigger the release of LY from the nanosystem, making the DNP-AuNPs-LY@Gel a stimuli-responsive drug delivery system.<sup>[30]</sup>

## 2.3. SERS Monitoring of Delivered LY in Living CRC Cells

The major shortcoming of existing diatomite-based nanovectors is their limited detection sensitivity that hinders the label-free monitoring and quantification of intracellular drug release. To overcome this limitation, hybrid systems made of diatoms and metal nanostructures have been proposed as SERS substrates.<sup>[43]</sup> The near-field optical amplification of metal nanostructures on diatoms increases their detection performance, allowing label-free sensing of biomolecules with excellent specificity and sensitivity.<sup>[44,45]</sup> The combination of the drug-loading capacity of DNPs with the strong Raman enhancement of molecules close to AuNPs is an ideal strategy to combine therapeutic purposes with label-free intracellular drug monitoring. Indeed, the hybrid nanosystem can integrate multiple functionalities allowing bio-imaging and drug delivery goals simultaneously without the use of any fluorophore or external marker, avoiding fluorescence-quenching issues.

In this study, the incorporation of LY into the DNP-AuNPs system and the enhancement of the LY signal were preliminarily evaluated by carefully studying the Raman and SERS spectra. **Figure 3a** compares the SERS signals of the complex DNP-AuNPs-LY@Gel (blue line), DNP-AuNPs@Gel (red line), and the substrate DNP-AuNPs alone (green line). Each spectrum was the average of 30 acquisitions. For reference, the Raman spectrum of the LY was shown (black line). The LY Raman spectrum was recorded on a drop of LY ( $5 \text{ mg mL}^{-1}$  in

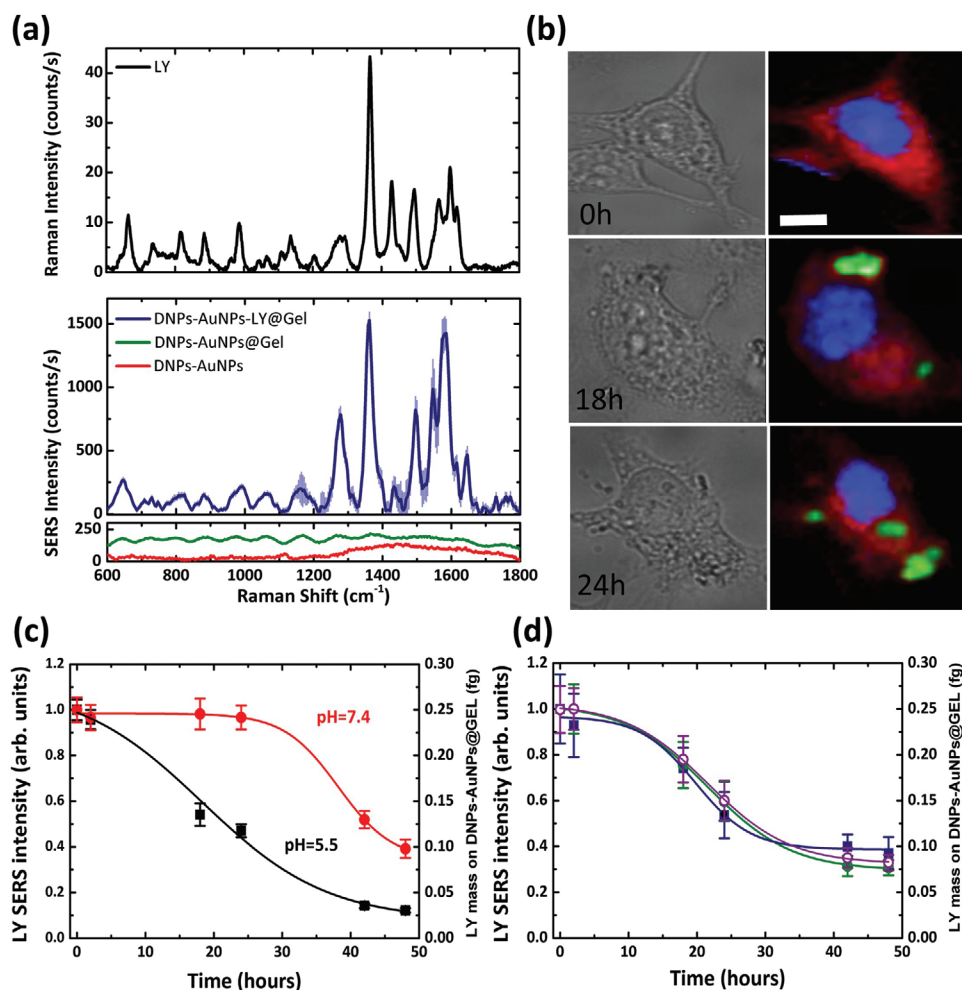


**Figure 3.** a) Raman spectrum of LY (black line). Experiments were carried out with laser wavelength 638 nm, laser power 20 mW, microscope objective 60X, integration time 1 s. The SERS spectrum of LY from 500  $\mu\text{g mL}^{-1}$  of the complex DNP-AuNPs-LY@Gel (blue line), the background signals from the DNP-AuNPs@Gel (red line) and the DNP-AuNPs alone (green line) were measured. Laser power: 1 mW. All the SERS and Raman spectra were rescaled to a common laser power of 1 mW so that the intensities could be directly compared. Spectra are offset for clarity. b) Optical image and Raman mapping images showing the internalization of DNP-AuNPs-LY@Gel (50  $\mu\text{g mL}^{-1}$ ) into CRC cells after 0, 18, and 24 h of incubation. Scale bar = 10  $\mu\text{m}$  c) Time-dependent LY SERS intensity from the DNP-AuNPs-LY@Gel complex and LY mass on the nanovector in PBS buffer at pH 7.4 and pH 5.5. d) Time-dependent LY SERS signal from the DNP-AuNPs-LY@Gel complex in living CRC cells.

acetone) deposited on the coverslip and left to dry to allow the total evaporation of the solvent. The Raman spectra of LY and acetone were reported in Figure S2 (Supporting Information), showing that there was no overlap of the characteristic Raman bands of LY and acetone. The LY Raman spectrum exhibited strong bands in the spectral region between 1300–1600  $\text{cm}^{-1}$  ascribed to the main molecular vibrational bonds of the pyridine (basically CH, CN, CC stretching and bending modes). A detailed LY Raman band assignment was reported in Table S1 (Supporting Information). The SERS fingerprint of the LY -markedly similar to its Raman counterpart- was observed from the complex DNP-AuNPs-LY@Gel and the tentative assignment of the vibrational modes was reported in Table S1 (Supporting Information). Control experiments were carried out on the DNP-AuNPs@Gel and the substrate DNP-AuNPs alone. Notably, the DNP-AuNPs@Gel and DNP-AuNPs SERS signal did not show any significant spectral feature in the regions between 1300–1650  $\text{cm}^{-1}$ , excluding major contributions to the

SERS signal of the substrate itself and other organic components of the nanovector, such as the dicarboxylic PEG or gelatin capping. Our measurements confirmed that the LY molecules strongly interacted with the metallic NPs and hotspots. Therefore, the most intense SERS vibration, ascribed to a combined action of ring C–N stretching and ring bending, was found at 1360  $\text{cm}^{-1}$ .<sup>[46–49]</sup> The intensity of this band was used for monitoring the LY intracellular release from the developed platform.

For SERS experiment, a drop (3  $\mu\text{L}$ ) of the DNP-AuNPs-LY@Gel dispersion (500  $\mu\text{g mL}^{-1}$ ); LY loaded was  $20 \pm 4 \mu\text{g}$  per mg of DNP-AuNPs-LY@Gel corresponding to  $\approx 25 \times 10^{-6} \text{ M}$  of LY) was deposited on a  $\text{CaF}_2$  slide. The SERS spectrum of the complex DNP-AuNPs-LY@Gel revealed an enhancement (SERS Gain, G) of the LY signal of about  $4.5 \times 10^5$ , further confirmed by the analysis of the Enhancement Factor (EF) of the proposed metallic substrate reported in the Supporting Information. G was calculated as the ratio between the SERS and Raman signal of the LY bands at 1360  $\text{cm}^{-1}$ , normalized to the power

(1 mW vs 20 mW), integration time (1 s), and concentration ( $25 \times 10^{-6}$  M vs  $15 \times 10^{-3}$  M) of the drug. G provided quantitative information on the signal gain expected from the DNP-AuNPs-LY@Gel complex with compared to the pure LY Raman measurement, assuming that all the experimental parameters, such as the objective, laser wavelength, and spectrometer were the same. This parameter had the advantage of being free from the overestimation error performed when calculating the probed molecules required for the evaluation of the EF reported in the Supporting Information.<sup>[50]</sup>

The SERS spectra of LY loaded in DNP-AuNPs-LY@Gel complex acquired within 30 s with an integration time of 1 s were reported in Figure S3a (Supporting Information). The spectra were well reproducible and the intensities on a selected nanocomplex could vary up to about 18% (the standard deviations for the band at 1360, 1500, 1545, and 1580  $\text{cm}^{-1}$  were respectively 4%, 11%, 18%, and 8%). The SERS intensity for the band at 1360  $\text{cm}^{-1}$  was about 1500 counts  $\text{s}^{-1}$  at the considered experimental parameters. A standard deviation of about 10% was registered for signals acquired on different clusters of the DNPs, showing a good inter-sample reproducibility (see Figure S3b, Supporting Information).

Before investigating the release properties of the DNP-AuNPs-LY@Gel nanovector, we evaluated its internalization in the human LS-174T CRC cell line by Raman imaging. Figure 3b shows the Raman map of the LS-174T cell incubated with a dispersion of 50  $\mu\text{g mL}^{-1}$  of DNPs-AuNPs-LY@Gel for 18 and 24 h and the control sample at 0 h. Different colors are associated with the loadings/spectra (see Figure S4, Supporting Information) used to reconstruct the Raman map and are linked with a specific cell location (i.e., nucleus, cytoplasm) or with the nanocomplex. By using the MCR approach, it was possible to reconstruct a false color Raman map of the cell showing that the nanovector was internalized and localized in few clusters distributed through the cell cytoplasm after 18 h of incubation.<sup>[28]</sup>

We next investigated the LY release from the DNP-AuNPs-LY@Gel nanosystem in two different pH environments, 5.5 and 7.4, by SERS analysis. To this aim, a drop (3  $\mu\text{L}$ ) of DNP-AuNPs-LY@Gel dispersion (500  $\mu\text{g mL}^{-1}$ ) was deposited on a  $\text{CaF}_2$  slide, with a concentration of 250  $\text{ng mm}^{-2}$  on a circular area of 20  $\text{mm}^2$ . The total mass of DNPs was 1.5  $\mu\text{g}$  corresponding to an amount of loaded LY of 30 ng, with an LY mass for a single DNP of 0.25 fg (see section Quantification of the LY release). The SERS investigations under different pH conditions were performed in parallel (Figure 3c). In physiological conditions (PBS, pH 7.4), a very small amount of LY (about 4%) was released by the DNP-AuNPs-LY@Gel complex within 24 h. A slow release was observed after 30 h and about 60% of LY was delivered from DNP-AuNPs-LY@Gel after 48 h. At pH 5.5, mimicking the cancer cell microenvironment, the release of LY from the nanovector became faster and a great amount of LY (about 50%) was released after 24 h, reaching 90% of the released drug after 48 h. These results confirmed that the gelatin coating provided the nanoplatform with a pH-responsive behavior and triggers the drug release in acidic conditions, as observed by HPLC analysis.<sup>[41]</sup>

To further demonstrate the accuracy of the nanosystem acting as SERS sensor, the DNP-AuNPs complex was incubated with four different concentrations of LY (25, 175, 12, and  $9 \times 10^{-6}$  M),

capped with gelatin, and the SERS signals of the loaded LY was investigated. The mean LY SERS spectra acquired before (black) and after (red) the release were reported in Figure S5a–c (Supporting Information). Before the release, the intensity of the band at 1360  $\text{cm}^{-1}$  was 1500 counts  $\text{s}^{-1}$ , 1000 counts  $\text{s}^{-1}$ , 750 counts  $\text{s}^{-1}$ , and 600 counts  $\text{s}^{-1}$  for the nanocomplex incubated with 25, 175, 12, and  $9 \times 10^{-6}$  M, respectively; after 48 h of release, the intensity was 150 counts  $\text{s}^{-1}$  for all samples. The SERS intensity of the control sample, i.e., the DNP-AuNPs@Gel complex without LY, was 30 counts  $\text{s}^{-1}$  at 1360  $\text{cm}^{-1}$ . These data reported in Figure S5d (Supporting Information) show that the SERS intensity was directly proportional to the LY concentration with a high value of  $R^2$  (0.997). From this curve, it was also extrapolated that the LY SERS intensity measured after 48 h of release (150 counts  $\text{s}^{-1}$ ) corresponded to about  $2 \times 10^{-6}$  M of LY. The SERS spectra of LY were well reproducible from  $25$  to  $2 \times 10^{-6}$  M and enabled to trace the release of LY in vitro.

The amount of LY released from the nanoplatform was quantified by SERS according to the nanoplatform loading capacity calculated by HPLC (Section 2.2). According to Figure 3c, about 50% of LY was released from 1.5  $\mu\text{g}$  of DNP-AuNPs-LY@Gel after 24 h in the acidic microenvironment, corresponding to about 0.125 fg per nanocomplex unit (about 15 ng overall of LY). These observations confirmed that the loaded anticancer drug was efficiently released in acidic conditions and that the release could be quantified per single nanocomplex unit thanks to the high sensitivity provided by the SERS technique.

We further investigated and quantified the time-dependent release of LY from the DNP-AuNPs-LY@Gel in living LS-174T cells by monitoring the LY SERS signal at various incubation time intervals (0, 2, 18, 24, 42, and 48 h). A dispersion of DNPs-AuNPs-LY@Gel was incubated in 1.5 mL of cell medium at a final concentration of 50  $\mu\text{g mL}^{-1}$ , corresponding to a total mass of DNPs-AuNPs-LY@Gel of 75  $\mu\text{g}$  and a total mass of LY loaded on DNPs of 1.5  $\mu\text{g}$ . The mass of LY for DNP unit was 0.25 fg. After 2 h, the SERS signal was collected only from DNPs not internalized in the cells and the LY signal intensity was comparable to the control experiments without cells. At this point, the nanoplatform was not yet internalized and it was not possible to trace the SERS signal of LY in cells. Conversely, after 18 h the nanoplatform penetrated cancer cells and the LY SERS signal was detected inside cells, indicating a successful internalization. After 18 h the amount of LY released in LS-174T cells was about 30% of the total drug encapsulated, corresponding to 450 ng of LY (0.075 fg for DNP unit). The released LY was about 50% of the total encapsulated drug (750 ng overall, 0.125 fg for DNP unit) after 24 h. A smooth LY release was observed after 30 h and about 65% of LY was released (975 ng overall, 0.16 fg for DNP unit) after 48 h. Interestingly, in this study, an efficient SERS intracellular tracing and imaging of LY in living CRC was demonstrated up to 48 h and quantified to provide LY sensing resolution down to  $7.5 \times 10^{-18}$  g. For comparison, the LY release from the DNP-AuNPs-LY complex (without the gelatin coating) was investigated in PBS pH 7.4 and pH 5.5 and in living CRC within 48 h by SERS analysis. A burst LY release of about 50% was observed after 60 s in all the release conditions (Figure S6, Supporting Information). The LY SERS signal completely disappeared after 10 min, in agreement with the in vitro release

tests investigated by HPLC (Figure S1, Supporting Information). These results further demonstrated that the nanosystem designed without the gelatin coating was not suitable for sustained drug delivery inside cancer cells.

#### 2.4. Evaluation of MET Induced by DNPs-AuNPs-LY@Gel in CRC Cells

After assessing the drug release properties of the developed nanoplatform, we evaluated whether the controlled delivery of LY from the DNP-AuNPs-LY@Gel complex could increase the therapeutic efficacy of the drug, reducing tumor cell invasiveness and metastasis.

For these studies, the LS-174T cell line was chosen due to its metastatic potential and mesenchymal phenotype.<sup>[51]</sup> The LS-174T cells were also selected because they trigger an intact TGF- $\beta$  signaling useful to test the inhibitory potential of LY delivered by our complex.<sup>[52]</sup> Firstly, the cellular uptake of DNP-AuNPs-LY@Gel labelled with Alexa Fluor 488 (DNP-AuNPs\*-LY@Gel) was investigated by confocal microscopy (Figure 4). To evaluate whether the gelatin layer affected the cellular uptake of the DNPs, the internalization of the labeled DNP-AuNPs-LY complex (DNP-AuNPs\*-LY) was investigated as well. To this aim, 50  $\mu\text{g mL}^{-1}$  of DNP-AuNPs\*-LY@Gel or DNP-AuNPs\*-LY were incubated with the LS-174T cell line for 24 h; cell nuclei and membranes were stained with DAPI and WGA-Alexa Fluor 555, respectively. Untreated cells (first line of Figure 4) and cells treated with free dye Alexa Fluor 488 (last line of Figure 4) are also shown as controls.

The images revealed that the presence of the gelatin layer did not alter the cellular uptake of the DNPs since both the DNP-AuNPs\*-LY@Gel and DNP-AuNPs\*-LY complex were characterized by a comparable internalization; these results were also in agreement with previous studies performed on different cell lines.<sup>[20,25,28,29]</sup> The morphological analysis performed on the cells reported in Figure 4 allowed to evaluate the mesenchymal to epithelial transition induced by the gelatin-coated and uncoated nanoplatform. The results, expressed in terms of elongated (mesenchymal) and rounded (epithelial) cells and reported as inset of the merge images, showed that only the DNPs-AuNPs\*-LY@Gel complex was able to promote the reversion of the cell phenotype. Moreover, since the internalization of DNPs with and without the gelatin layer was comparable, the lower phenotype reversion observed with the DNP-AuNPs\*-LY complex can be ascribed to the LY release from the nanosystem before its internalization in cells.

The biocompatibility of the DNPs-AuNPs@Gel suspension was investigated by exposing the LS-174T cell line to the nanosystem at different concentrations (12.5, 25, 50, and 100  $\mu\text{g mL}^{-1}$ ) for 24 and 48 h and monitoring the cell growth. The results reported in Figure S7a (Supporting Information) demonstrated that the multifunctional platform did not induce cell toxicity after 48 h up to a concentration of 50  $\mu\text{g mL}^{-1}$ , which was considered optimal for cell treatments. The cell growth of LS-174T was also investigated in presence of  $2.5 \times 10^{-6}$  M of LY, 50  $\mu\text{g mL}^{-1}$  of DNPs-AuNPs@Gel or DNPs-AuNPs, and 50  $\mu\text{g mL}^{-1}$  of DNPs-AuNPs-LY@Gel or DNPs-AuNPs-LY (both containing  $2.5 \times 10^{-6}$  M of LY, according to the

HPLC quantitative analysis reported in Section 2.2) (Figure 5a and Figure S7b: Supporting Information). We did not observe significant changes in cell growth after 48 h upon treatment with all the indicated nanoplatforms in the LS-174T cell line, demonstrating that also the nanoplatform loaded with LY can be considered safe.

For comparison, analogue studies were performed using the SW620 cell line, highly invasive colon cancer cells that display similar phenotype and genetic background of LS-174T cells.<sup>[52]</sup> In this case, we observed a slight increase in cell growth in the presence of DNPs-AuNPs@Gel, DNPs-AuNPs and DNPs-AuNPs-LY suspensions (Figure 5b and Figure S7c: Supporting Information). Overall, we observed that none of the components of the developed nanoplatform was toxic for the cells.

It has been shown that MET may be induced by blocking the activity of specific factors and signaling pathways that trigger EMT, including the TGF- $\beta$ -mediated phosphorylation of SMAD proteins.<sup>[53]</sup> The TGF- $\beta$  signaling pathway is a well-characterized factor involved in EMT and the development and progression of tumor metastasis. In CRC disease, the EMT is associated with an invasive and metastatic phenotype and the inhibition of the TGF- $\beta$  signaling has been considered a valid strategy to halt EMT and enhance MET.<sup>[54]</sup> Therefore, we investigated whether the DNP-AuNPs-LY@Gel platform could directly reverse EMT by blocking the TGF- $\beta$ 1 receptor. The anti-metastatic effect of the developed hybrid multifunctional complex was assessed by investigating *E-CADHERIN*, *SNAIL-1*, and *TWIST-1* levels in LS-174T and SW620 cells using quantitative PCR (qPCR) analysis. MET is characterized by loss of mesenchymal markers (i.e., *SNAIL-1* and *TWIST-1*) and, in turn, enhancement of epithelial markers (i.e., *E-CADHERIN*).<sup>[55]</sup> During the EMT, the cells lose their epithelial characteristics, like cell polarity and cell-cell contacts, and gain mesenchymal traits such as increased motility.<sup>[56]</sup> The transient nature of the EMT events allows mesenchymal cells to revert to an epithelial shape when signals driving the EMT decrease. In both cell lines, the DNP-AuNPs-LY@Gel complex significantly increased the expression of *E-CADHERIN* and suppressed the expression of *SNAIL-1* and *TWIST-1* genes (Figure 5c,d). Of note, the modulation of the expression levels of *E-CADHERIN*, *SNAIL-1*, and *TWIST-1* genes was much stronger upon treatment with DNP-AuNPs-LY@Gel than free LY at equal concentration. The encapsulation of LY in the hybrid nanoplatform (covered with gelatin) allowed lowering the LY dose necessary to induce MET in metastatic cells. Reduced doses can also help prevent adverse side effects and risks related to the circulation of toxic metabolites in the plasma. Any gene modulation was not observed after treatment with DNPs-AuNPs@Gel, DNPs-AuNPs, and DNPs-AuNPs-LY suspensions (Figure 5c,d and Figure S7d,e: Supporting Information). These results confirmed that the gene modulation is observed only upon exposure to the nanocomplex containing LY; the DNPs-AuNPs-LY complex realized without the gelatin layer did not induce any variation because it was not able to retain LY as demonstrated by HPLC (Figure S1, Supporting Information) and SERS (Figure S6, Supporting Information) analyses. Furthermore, since *E-CADHERIN* plays an essential role in maintaining epithelial integrity, its upregulation was also accompanied by morphological changes in both LS-174T and SW620 cells as observed in Figure 5e.

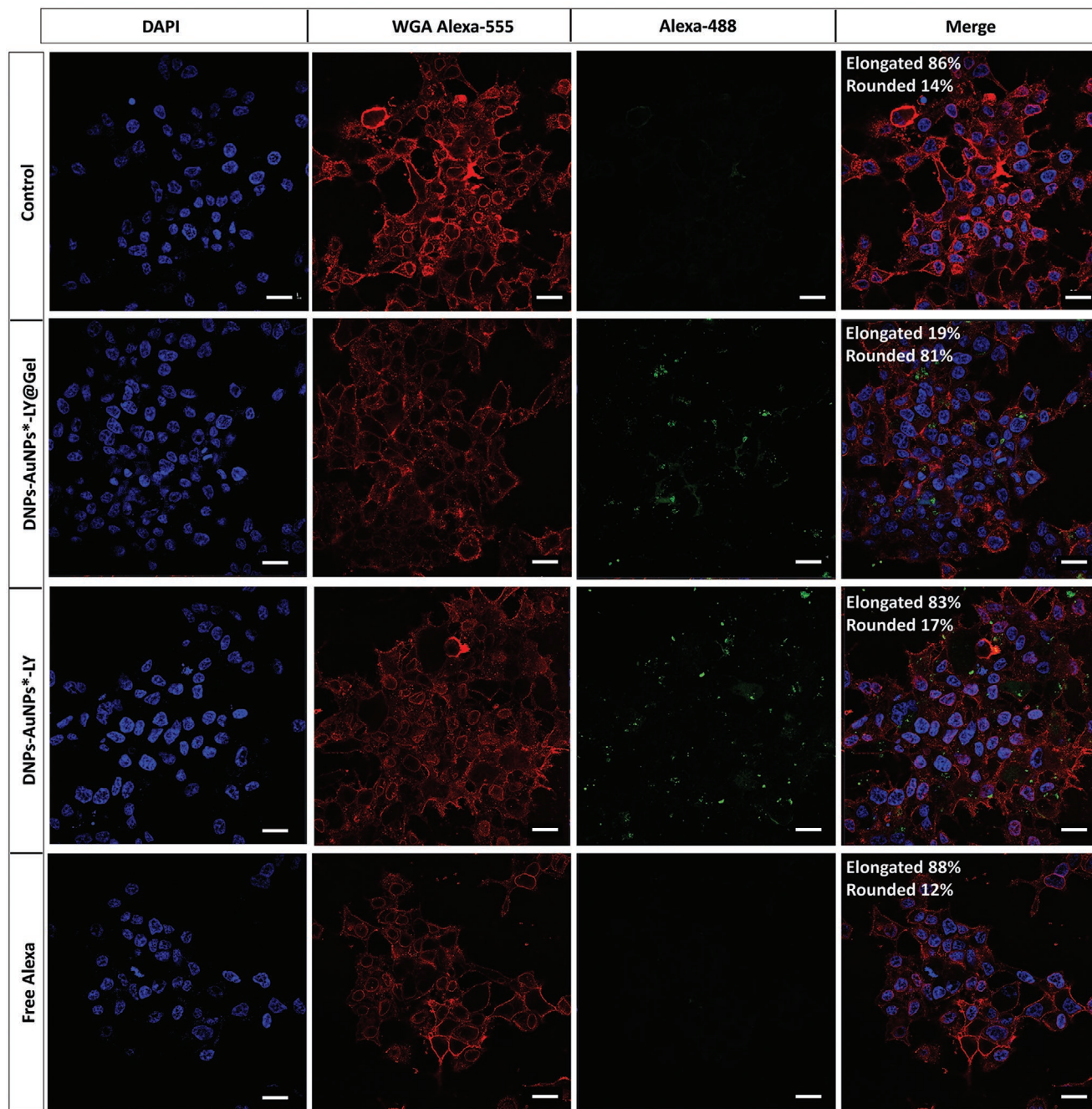


**Figure 4.** Representative confocal fluorescence images of LS-174T cells incubated for 24 h with  $50 \mu\text{g mL}^{-1}$  of labelled DNPs-AuNPs-LY@Gel (DNPs-AuNPs\*-LY@Gel) or DNPs-AuNPs-LY (DNPs-AuNPs\*-LY). As a control, untreated cells (first line) and cells treated with the free dye Alexa Fluor 488  $20 \mu\text{g mL}^{-1}$  (last line) were also reported. Cell nuclei and membranes were stained with DAPI and WGA-Alexa Fluor 555, respectively; the DNPs were labelled with Alexa Fluor 488 via carbodiimide chemistry. Scale bar =  $20 \mu\text{m}$ .

Specifically, cells treated with a suspension of  $50 \mu\text{g mL}^{-1}$  of DNPs-AuNPs-LY@Gel showed an evident morphological shift from elongated and spindle-shape (mesenchymal) to rounded (epithelial) phenotype after 48 h compared to untreated or treated with DNPs-AuNPs@Gel or DNPs-AuNPs-LY cells (Figure 5e and Figure S7g, Supporting Information). The morphological changes were quantified recording the phenotype shapes over time (from 0 to 48 h) (Figure 5f). The transition

from elongated to rounded phenotype was already appreciable after 24 h of treatment with DNP-AuNPs-LY@Gel complex and it became stronger after 44 h since 60% of the cells lost mesenchymal phenotype. The complete phenotype reversion occurred after 48 h of incubation in both cell lines, where 80% of cells acquired epithelial morphology (Figure 5f). The cell evolution to a rounded phenotype follows the same profile as the intracellular drug release evaluated by SERS analysis (section 2.3). Data

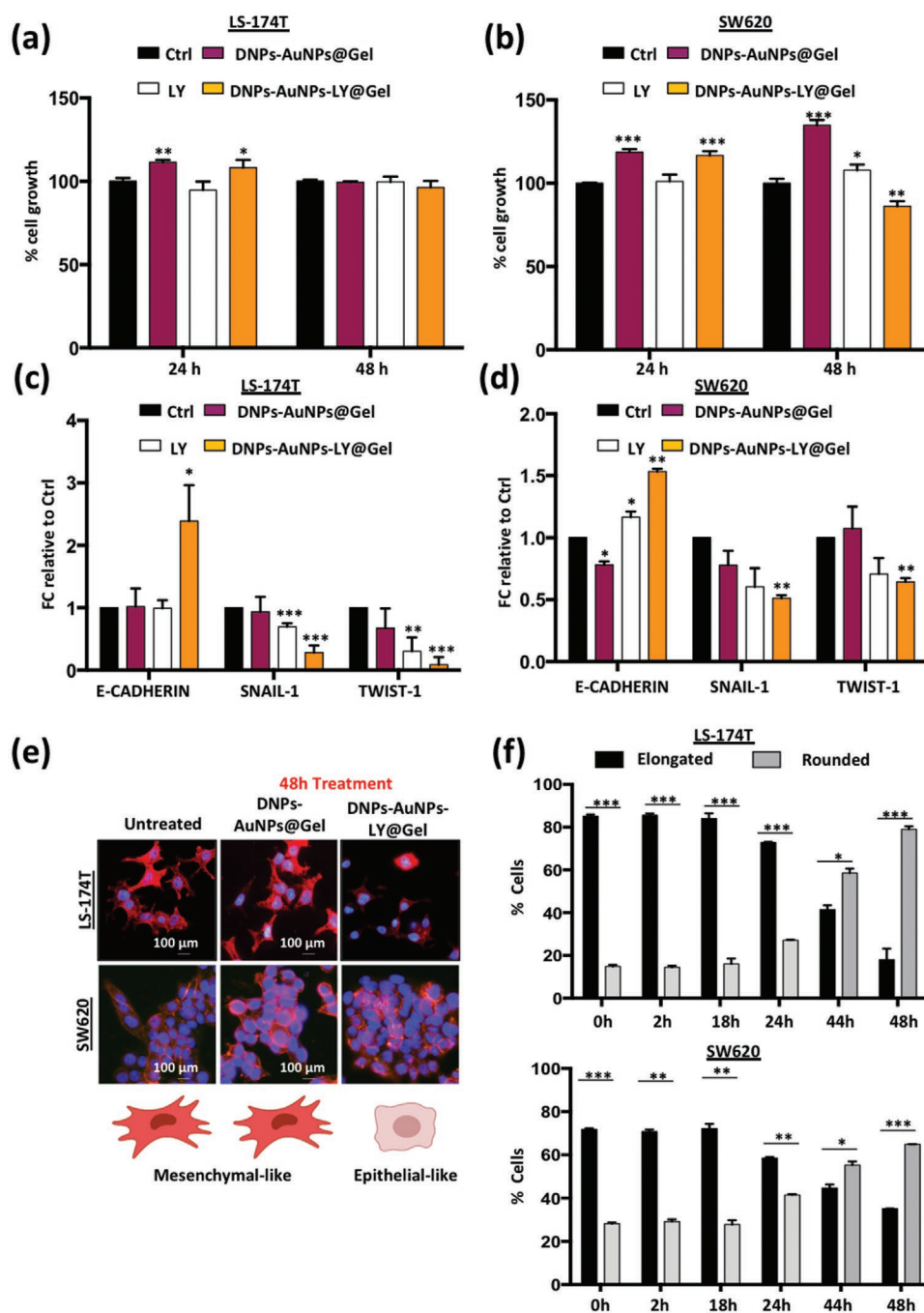


**Figure 5.** a) Cell viability of LS-174T cells grew for 24 and 48 h in the presence or absence of  $2.5 \times 10^{-6}$  M LY,  $50 \mu\text{g mL}^{-1}$  of DNPs-AuNPs@Gel, and  $50 \mu\text{g mL}^{-1}$  of DNPs-AuNPs-LY@Gel (containing  $2.5 \times 10^{-6}$  M of LY). Cell viability was evaluated using CCK8, and absorbance was measured at 450 nm.  $*p < 0.05$ ,  $**p < 0.005$ ,  $***p < 0.0005$ .  $n \geq 6$ . b) Cell viability of SW620 cells grew for 24 and 48 h in the presence or absence of  $2.5 \times 10^{-6}$  M LY,  $50 \mu\text{g mL}^{-1}$  of DNPs-AuNPs@Gel, and  $50 \mu\text{g mL}^{-1}$  of DNPs-AuNPs-LY@Gel (containing  $2.5 \times 10^{-6}$  M of LY). Cell viability was evaluated using CCK8, and absorbance was measured at 450 nm.  $*p < 0.05$ ,  $**p < 0.005$ ,  $***p < 0.0005$ .  $n \geq 6$ . c) qPCR analysis of EMT genes in LS-174T cells grew for 24 h in presence of  $2.5 \times 10^{-6}$  M LY,  $50 \mu\text{g mL}^{-1}$  of DNPs-AuNPs@Gel, and  $50 \mu\text{g mL}^{-1}$  of DNPs-AuNPs-LY@Gel (containing  $2.5 \times 10^{-6}$  M of LY). Data were normalized to *GAPDH* expression and presented as Fold Change (FC) in gene expression relative to control (Ctrl).  $*p < 0.05$ ,  $**p < 0.005$ ,  $***p < 0.0005$ .  $n \geq 6$ . d) qPCR analysis of EMT genes in SW620 cells grew for 24 h in presence of  $2.5 \times 10^{-6}$  M LY,  $50 \mu\text{g mL}^{-1}$  of DNPs-AuNPs@Gel, and  $50 \mu\text{g mL}^{-1}$  of DNPs-AuNPs-LY@Gel (containing  $2.5 \times 10^{-6}$  M of LY). Data were normalized to *GAPDH* expression and presented as Fold Change (FC) in gene expression relative to control (Ctrl).  $*p < 0.05$ ,  $**p < 0.005$ ,  $***p < 0.0005$ .  $n \geq 6$ . e) Representative images of DNPs-AuNPs-LY@Gel-mediated MET in LS-174T and SW620 cells. f) Percentage of cells with elongated (mesenchymal) or rounded (epithelial) shape treated with DNPs-AuNPs-LY@Gel ( $50 \mu\text{g mL}^{-1}$ ) at the indicated times. The number of counted cells “n” is  $\geq 500$ .  $*p < 0.05$ ,  $***p < 0.0005$ .  $n \geq 5$ .

compared in Figure S8 (Supporting Information) confirmed the ability of the developed nanoplatform to provide a precise dose-response profile by correlating the amount of the internalized drug and cell outcome. Moreover, the observed morphological changes confirmed that the metastatic process could be slackened by treating the CRC cells with the developed nanoplatform which turns out to be more efficient if covered with gelatin.

Finally, we studied the effects of the LY delivery on normal human colon epithelial cells (CRL-1790) upon exposure to  $50 \mu\text{g mL}^{-1}$  of the DNP-AuNPs-LY@Gel or DNP-AuNPs-@Gel complex.<sup>[57]</sup> The treatment with DNP-AuNPs-LY@Gel did not induce effects on the normal cell line since the expression levels of *SNAIL-1* and *TWIST-1* genes were unvaried (Figure S7f, Supporting Information). However, since the normal cells are generally responsive to TGF- $\beta$  signaling, we cannot exclude that some other genes, not discussed in this study, could be affected by the treatment with the DNP-AuNPs-LY@Gel complex.

In conclusion, even if the DNP-AuNPs-LY@Gel nanosystem exhibited the ability to revert the metastatic process in CRC cells, it is worth considering the administration of LY and a cancer-cytotoxic agents to block the metastasis and reduce the tumour growth simultaneously.<sup>[58,59]</sup>

### 3. Conclusions

Here, for the first time, we describe the production of a plasmonic-assisted nanoplatform for the real-time monitoring of Galunisertib release in colorectal cancer cells. The ability of gold NPs to enhance the SERS signal of Galunisertib loaded in the DNP was efficiently exploited to trace and quantify the release of the small molecule in living cells over days. Galunisertib was loaded in the DNP with a loading capacity of  $20 \mu\text{g mg}^{-1}$  and the nanoplatform was capped by a thin layer of gelatin, overcoming the common burst release effect of porous drug carriers. In vitro release studies showed that the DNP-AuNPs-LY@Gel nanoplatform exhibited a pH-responsive release of Galunisertib starting at  $\text{pH} < 6$ . The gelatin shell provided the possibility to prevent burst release effects, enhance the LY delivery in cells and control the LY release in malignant cells, where the acidic microenvironment and the overexpression of MMP-2 enzymes promoted the gelatin degradation. The drug release profile investigated by either HPLC and SERS techniques revealed that SERS is a high-sensitive and reliable method for the investigation and quantification of drug release profiles. Significantly, the SERS enhancement of Galunisertib signals in the DNP-AuNPs-LY@Gel platform allowed extreme sensitivity down to sub-femtogram of the drug, enabling the label-free monitoring of drug release in living cells. The biocompatibility was demonstrated in vitro in both LS-174T and SW620 cancer cell lines, showing that the DNP-AuNPs-LY@Gel treatment was safe up to a concentration of  $50 \mu\text{g mL}^{-1}$ . The modulation of the expression levels of *E-CADHERIN*, *SNAIL-1*, and *TWIST-1* genes upon treatment with the nanoplatform was significantly higher than free Galunisertib. Moreover, the antimetastatic effect was further demonstrated by confocal microscopy, revealing that the shape of LS-174T cells efficiently turned from mesenchymal to epithelial-like phenotype in the presence

of the multifunctional platform. These studies showed that the encapsulation of Galunisertib in the developed nanoplatform can help lowering the amount of drug required to inhibit the metastatic process in cancer cells, reducing the formation of drug-related toxic metabolites.

### 4. Experimental Section

**Chemicals and Reagents:** Diatomite was obtained by DERE SPA (Castiglione in Taverina, Viterbo, Italy); 1-ethyl-3-[3-dimethylaminopropyl] carbodiimide-hydrochloride/N-hydroxysuccinimide (EDC/NHS), 3-aminopropyltriethoxysilane (APTES), type-B gelatin, 2-(N-Morpholino) ethane sulfonic acid hemisodium salt (MES), tetrachloroauric acid ( $\text{HAuCl}_4$ ), dicarboxylic polyethylene glycol (PEG 600), sodium tetrahydridoborate ( $\text{NaBH}_4$ ), sulfuric acid ( $\text{H}_2\text{SO}_4$ ), Biphenyl-4-Thiol (BPT), Trifluoroacetic Acid (TFA), poly-L-lysine, and acetone HPLC grade were purchased from Merck KGaA (DE). Phosphate Buffered Saline IX (PBS) and Dulbecco Modified Eagle Medium (DMEM) were purchased from GIBCO (IE). Chloride acid (HCl) was purchased from Romil (UK). Wheat Germ Agglutinin (WGA) Alexa Fluor 555 conjugate, Alexa Fluor 488, and 4',6-diamidin-2-phenylindole (DAPI) were purchased from Invitrogen, Thermo Fisher Scientific (USA). Absolute ethanol (EtOH), sodium chloride (NaCl), and hydrogen peroxide ( $\text{H}_2\text{O}_2$ ) were purchased from Carlo Erba (IT). Galunisertib (LY 2157299) was purchased from Axon Medchem (NL). Fetal Bovine Serum (FBS) and Trypsin-EDTA were purchased from Euroclone (IT). Paraformaldehyde (PFA) was purchased from Himedia (DE). Penicillin and Streptomycin were purchased from Aurogene (IT).

**Preparation of the DNP-AuNPs-LY@Gel Nanosystem:** DNPs were obtained by mechanical crushing, sonication and purification of natural diatomite powder, according to methods previously described<sup>[20]</sup>. DNPs (1 mg) were amino-modified by 10% v/v APTES solution in absolute EtOH (1 mL). The silanization process was carried out for 30 min under vigorous stirring at room temperature. The DNP dispersion was centrifuged, and the supernatant was removed. Amino-modified DNPs underwent a curing process for 1 h at  $40^\circ\text{C}$  washed with EtOH and collected. The next steps required for the preparation of the nanosystem were sketched in Figure S9 (Supporting Information). (I) Synthesis of gold-decorated-DNP complex (DNP-AuNPs): DNP-AuNPs complex was obtained by dispersing amino-modified DNPs ( $125 \mu\text{g}$ ) in chloroauric acid ( $\text{HAuCl}_4$ ,  $1 \times 10^{-3} \text{ M}$ ) aqueous solution (2.5 mL) and mixing under mild stirring for 10 min at room temperature. To this solution, dicarboxylic polyethylene glycol (PEG, 0.2 mL) was added and vigorously mixed for 5 min. Finally, sodium borohydride ( $\text{NaBH}_4$ , 0.1 M,  $150 \mu\text{L}$ ) in aqueous solution was added at once. The color of the dispersion instantly changed from yellow to red when  $\text{NaBH}_4$  was added to the solution confirming the formation of AuNPs on the surface of the DNP. The as-prepared dispersion of DNPs-AuNPs was centrifuged to remove the excess reagents at 3,500 rpm for 10 min, the supernatant was discarded, and the residue vigorously washed with Milli-Q water. (II) Drug loading: For drug loading, DNP-AuNPs ( $100 \mu\text{g}$ ) were soaked in a 10% acetone solution (1 mL) of Galunisertib 5-fold more concentrated than the carrier and gently mixed at  $\text{pH} 2.5$  for 2 h at  $37^\circ\text{C}$ . The drug loading solution was centrifuged at 3,500 rpm for 10 min and the supernatant with the unloaded drug was discarded. (III) Gelatin capping: To synthesize gelatin-covered NPs, a dispersion of DNPs-AuNPs-LY complex was mixed with a gelatin solution (1:2 weight ratio, respectively) in MES buffer ( $10 \times 10^{-3} \text{ M}$ , 1 mL)  $\text{pH} 3.5$  at  $50^\circ\text{C}$  for 2 h. For gelatin crosslinking, EDC ( $0.36 \times 10^{-6} \text{ M}$ ) and NHS ( $0.086 \times 10^{-6} \text{ M}$ ) were added to the above solution and gently stirred for 2 h at  $37^\circ\text{C}$ . The weight ratio between gelatin, EDC, and NHS was 1:1.4:0.2, respectively. After crosslinking, the gelatin-covered DNP-AuNPs-LY system (DNPs-AuNPs-LY@Gel) was vigorously washed with Milli-Q water and collected in water.

**Dynamic Light Scattering (DLS):** Hydrodynamic diameter and surface  $\zeta$ -potential of bare ( $50 \mu\text{g}$ ) and modified DNPs ( $50 \mu\text{g}$ ) were measured in

water using a Zetasizer Nano-ZS instrument (Malvern Instrument Ltd, UK) equipped with a He-Ne laser (633 nm, scattering angle of 90°, 25 °C). Data reported in Section 2.1 were the mean of five measurements. The size distributions of DNPs, DNPs-AuNPs, and DNPs-AuNPs-LY@Gel samples determined by DLS measurements were reported in Figure S10 (Supporting Information).

**Transmission Electron Microscopy (TEM):** The morphology of the DNP was investigated before and after surface modifications using a transmission electron microscope (TEM, Jeol JEM-1400, Jeol Ltd, Japan). Samples were prepared in water at a concentration of 500 µg mL<sup>-1</sup> and dropped on a carbon-coated copper TEM grid before air-drying overnight at room temperature.

**UV-Vis Spectroscopy:** Absorption spectra of amino-modified DNP, DNP-AuNPs and DNP-AuNPs-LY@Gel complex dispersed in de-ionized water were recorded on Cary 100 UV-Vis double beam spectrophotometer (Agilent, CA, United States) using quartz cells of 10 mm path length and 0.5 mL total volume capacity.

**Fourier Transform Infrared Spectroscopy (FTIR):** Fourier transform infrared spectroscopy (FTIR) spectra of DNP before and after surface modifications were recorded by a Nicolet Continuum XL (Thermo Scientific) equipped with a microscope, in the range 3500–750 cm<sup>-1</sup> at a resolution of 4 cm<sup>-1</sup>.

**Drug Loading and Release Studies:** The drug loading capacity of modified-DNP was determined by immersing the DNP-AuNPs-LY@Gel complex (0.1 mg) into PBS (1 mL) pH 5.5 for 60 h under mild stirring. NPs were removed by centrifugation and the drug released in the supernatant was quantified by Reverse Phase-High Performance Liquid Chromatography (RP-HPLC) using a Shimadzu C<sub>18</sub> Column as stationary phase (5 µm particle size, 250 × 4.6 mm). Mobile phase A was an aqueous solution with trifluoroacetic acid (TFA, 0.02% v/v) and mobile phase B was acetonitrile with TFA (0.02% v/v). Samples were separated using the following gradient: 0–20 min (5% B → 95% B), 20–23 min (95% B), 23–43 min (95→5% B) with flow rate and wavelength set to 1 mL min<sup>-1</sup> and 254 nm, respectively. The amount of drug was quantified using an external calibration method and the drug loading capacity was determined by the following Equation (1):

$$\%LC = \frac{\text{amount of drug released (mg)}}{\text{amount of NPs (mg)}} \times 100 \quad (1)$$

In vitro release tests were performed by gently shaking DNP-AuNPs-LY@Gel (0.1 mg) in PBS (1 mL) pH 5.5 and 7.4 at 37 °C. At predetermined time intervals, the release solution was centrifuged at 3500 rpm for 5 min, the supernatant was collected and replaced with fresh PBS until the subsequent sampling time. The collected supernatants were filtered through syringe-filter 0.22 µm (Millex-GS, Merck, Darmstadt, Germany) and analysed by RP-HPLC according to the above-described method. The cumulative percentage release was calculated by using the Equations (2) and (3):

$$\text{Release \%} = \frac{\text{drug concentration at } t \text{ time}}{\text{total drug loaded}} \times 100 \quad (2)$$

$$\text{Cumulative release \%} = P(t-1) + Pt \quad (3)$$

where Pt = percentage release at time t and P(t-1) = percentage release at a previous time to t.

**Raman and SERS Microscopy:** Raman and SERS spectra and imaging were obtained from an inverted confocal Raman microscope (Xplora Inv, Horiba – Jobin Yvon, equipped with three laser lines at 532, 638, and 785 nm) using the laser line at 638 nm (50 mW, He-Ne) as the pump wavelength and a 60x water immersion objective lens (Nikon, NA = 1.2, WD = 300 µm). The slit aperture of the spectrometer was 100 µm, and the confocal pinhole was 100 µm. Rayleigh backscattered light was filtered out with a notch filter. The beam waist was measured with a knife-edge method detecting the Raman band at 514 cm<sup>-1</sup> of a Si-wafer blade and provided the value of about 0.7 µm at 638 nm.

For Raman imaging, 12-mm-diameter calcium fluoride (CaF<sub>2</sub>) coverslips used as optical substrates, were incubated with poly-L-lysine (0.01% v/v) for 10 min at room temperature to promote cell adhesion. Then, LS-174T cells were plated on the top of the coverslips and after 24 h a dispersion of DNPs-AuNPs-LY@Gel (50 µg mL<sup>-1</sup>) was added into wells in duplicate and incubated for 12 and 24 h at 37 °C. Before acquiring a Raman image of the sample, LS-174T cells were washed with PBS 3 times, fixed with PFA (2% v/v) for 10 min at room temperature and, finally, washed with PBS 3 times.

The Raman image was recorded by raster scanning the fixed cell through the laser focus (638 nm, laser power 20 mW), with a step size of 0.5 µm, and acquiring a 2D array of Raman spectra on a selected area (exposure time 0.5 s per spectrum). A total of 1500/2000 spectra for each cell were collected. The chemical maps (false colour Raman images) were generated using the multivariate curve resolution-alternative least square (MCR-ALS) method (HORIBA Scientific Lab Spec 6 software, Horiba Jobin Yvon, Villeneuve d'Ascq, France) [27].

For LY Raman spectroscopy, a drop (3 µL) of LY solution in acetone (5 mg mL<sup>-1</sup>) was deposited on a CaF<sub>2</sub> and dried. The LY Raman spectrum was acquired by using a laser at 638 nm, with laser power of 40 mW and acquisition time of 1 s. A drop (3 µL) of DNPs-AuNPs-LY@Gel (500 µg mL<sup>-1</sup>) dispersion was deposited on a CaF<sub>2</sub> coverslip and allowed to dry. The SERS spectrum of LY was recorded by using a laser power of 1 mW and an acquisition time of 1 s.

For live-cell SERS experiments, cells were seeded in 35 mm dishes and the day after were incubated with a dispersion of DNPs-AuNPs-LY@Gel (50 µg mL<sup>-1</sup>) in phenol red-free DMEM (500 µL) for 0, 2, 18, 24, 42, and 48 h. At each time point, SERS spectra of LY inside cells were acquired, by using a laser power of 1 mW and acquisition time of 1 s. The LY release was monitored by analyzing the intensity of the band at 1380 cm<sup>-1</sup>. For each time, SERS spectra were collected from 30 cells and the experiment repeated 3 times.

**SERS Gain:** To provide an estimation of the advantage of the complex DNP-AuNPs-LY SERS signal compared to the Raman one, the SERS gain “G” was analyzed. G was calculated as the ratio of the SERS signal intensity for the LY band at 1360 cm<sup>-1</sup> (I<sub>SERS</sub>) and the Raman intensity of the same band (I<sub>Raman</sub>), normalized to the different powers (P<sub>SERS</sub>, P<sub>Raman</sub>), integration times (t<sub>SERS</sub>, t<sub>Raman</sub>) and molecular concentrations (C<sub>SERS</sub>, C<sub>Raman</sub>):

$$G = \frac{\frac{I_{SERS}}{(t_{SERS} \times P_{SERS} \times C_{SERS})}}{\frac{I_{Raman}}{(t_{Raman} \times P_{Raman} \times C_{Raman})}} \quad (4)$$

**Quantification of the LY Release from DNP-AuNPs-LY@Gel Nanosystem by SERS:** 1) Investigation of LY release in PBS solution: A drop of the DNP-AuNPs-LY@Gel dispersion in PBS (3 µL, 500 µg mL<sup>-1</sup>) was deposited on a CaF<sub>2</sub> slide. The DNPs-AuNPs-LY@Gel suspension uniformly covered a circular area of 20 mm<sup>2</sup> (radius 2.5 mm), ensuring a concentration of 250 ng mm<sup>-2</sup>. The area occupied by a single cluster of DNP-AuNPs-LY@Gel was about 1 µm<sup>2</sup>, with a total mass of 75 fg and an overall LY mass of 1.5 fg.

A single DNP-AuNPs-LY@Gel particle had a radius of 225 nm and an area of 0.16 µm<sup>2</sup>, so for each cluster (1 µm<sup>2</sup>) ≈ 6 DNPs were there. Each DNP had a mass of about 12 fg, and LY mass was 0.25 fg, for DNP unit. Given the molecular weight of LY (369.42 g mol<sup>-1</sup>), 10<sup>6</sup> molecules of LY on a single cluster at T<sub>0</sub> was estimated.

$$\text{mass}_{LY} T_0 = 0.25 \text{fg} \quad (5)$$

After deposition and drying, the DNP-AuNPs-LY@Gel were completely immersed in two different PBS solutions (5.5 pH and 7.4 pH) respectively. LY SERS spectra were recorded at different times up to 48 h using a 638 nm laser. From the drug release curves, it was possible to estimate the residual LY mass on the single DNP after 48 h as below:

$$\text{mass}_{\text{LY}}T_{48}(\text{pH}7.4) = 0.1 \text{ fg} \quad (6)$$

$$\text{mass}_{\text{LY}}T_{48}(\text{pH}5.5) = 0.025 \text{ fg} \quad (7)$$

2) Time-dependent drug release investigations in CRC cells: A dispersion of DNPs-AuNPs-LY@Gel was incubated in the cell medium (1.5 mL in a 35 mm Petri dish) at a final concentration of  $50 \mu\text{g mL}^{-1}$ , corresponding to a total mass of DNP of  $75 \mu\text{g}$  and an overall mass of LY loaded of  $1.5 \mu\text{g}$ . The mass of LY for DNP unit was  $0.25 \text{ fg}$ . The analysis was recorded at different intervals for 48 h using a 638 nm laser. According to the drug release investigations in living cells, it was possible to estimate the residual LY mass on the single DNP as below:

$$\text{mass}_{\text{LY}}T_0 = 0.25 \text{ fg} \quad (8)$$

$$\text{mass}_{\text{LY}}T_{48}(\text{cells}) = 0.09 \text{ fg} \quad (9)$$

**Cell Culture:** The human colon cancer cell lines LS-174T and SW620, obtained from ATCC (American Type Culture Collection, Rockville, Maryland) were cultured in Dulbecco's Modified Eagle Medium (DMEM), supplemented with fetal bovine serum (FBS, 10% v/v) and penicillin/streptomycin ( $50 \text{ units mL}^{-1}$ ) at  $37^\circ\text{C}$  in a 5%  $\text{CO}_2$  atmosphere. The human normal colonic cells CRL-1790, obtained from ATCC were cultured in Eagle's Minimum Essential Medium (EMEM) supplemented with FBS (10% v/v) and penicillin/streptomycin ( $50 \text{ units mL}^{-1}$ ) at  $37^\circ\text{C}$  in a 5%  $\text{CO}_2$  atmosphere. All the experiments were conducted by plating cells at the density of  $30 \times 10^3$  cells/well in serum-free DMEM for 24 h, to reduce basal cellular activity.

For gene expression analysis, LS-174T, SW620, and CRL-1790 cells were seeded in a 24-well plate and after 24 h the cells were treated with LY ( $2.5 \times 10^{-6} \text{ M}$ ), a dispersion of DNPs-AuNPs-LY ( $50 \mu\text{g mL}^{-1}$ ), DNPs-AuNPs-LY@Gel ( $50 \mu\text{g mL}^{-1}$ ), DNPs-AuNPs ( $50 \mu\text{g mL}^{-1}$ ) and DNPs-AuNPs@Gel ( $50 \mu\text{g mL}^{-1}$ ) in serum-free media for 24 h. Lastly, the cells were harvested by EDTA-trypsin, washed twice with PBS, and collected by centrifugation.

**RNA Preparation and Real-Time PCR:** Total RNAs from human colon cancer cell were extracted with Eurogold TRIFAST kit (Euroclone) according to the manufacturer's instructions. One microgram of total RNA was used for cDNA synthesis with High-Capacity reverse transcriptase (ThermoFisher). Quantitative real-time PCR (qPCR) was performed using SYBR Green PCR master mix (ThermoFisher), according to the manufacturer's instructions. The list of utilized primers is depicted in Table S2 (Supporting Information).

**Cell Growth and Chemoresistance Assay:** Cells were treated with DNP-AuNPs-LY@Gel dispersion ( $12.5$ ,  $25$ ,  $50$ , and  $100 \mu\text{g mL}^{-1}$ ), DNP-AuNPs-LY ( $50 \mu\text{g mL}^{-1}$ ), DNPs-AuNPs ( $50 \mu\text{g mL}^{-1}$ ), DNPs-AuNPs@Gel ( $50 \mu\text{g mL}^{-1}$ ) and with LY ( $2.5 \times 10^{-6} \text{ M}$ ) for 24 and 48 h. Cell viability was determined using the CCK-8 assay kit according to the manufacturer's instruction (Dojindo).

**Confocal Fluorescence Imaging:** For confocal microscopy, the DNP-AuNPs complex was labelled to Alexa Fluor 488 via carbodiimide chemistry. DNPs-AuNPs ( $100 \mu\text{g}$ ) were dispersed in an Alexa Fluor 488 PBS solution ( $20 \mu\text{g mL}^{-1}$ ) and gently shaken in the presence of EDC ( $3.5 \times 10^{-6} \text{ M}$ ) and NHS ( $0.3 \times 10^{-6} \text{ M}$ ) for 90 min at room temperature. The coupling reaction promoted the peptide bond between the  $\text{NH}_2$  group of the fluorophore and the COOH groups of pegylated AuNPs decorating the surface of the nanosystem. Then, the Alexa-labelled DNP-AuNPs complex (DNP-AuNPs\*) was loaded with LY and capped by crosslinked gelatin according to the aforementioned procedure (DNP-AuNPs\*-LY@Gel).

For microscopy imaging, 12-mm glass coverslips were incubated with poly-L-lysine (0.01% v/v, 0.2 mL) for 10 min at room temperature (RT) to promote cell adhesion. LS-174T cells ( $5 \times 10^4$ ) were plated on the top of the coverslips and after 24 h DNP-AuNPs\*-LY ( $50 \mu\text{g mL}^{-1}$ ) and DNP-AuNPs\*-LY@Gel ( $50 \mu\text{g mL}^{-1}$ ) were added into wells with serum-free DMEM and incubated for 24 h at  $37^\circ\text{C}$ . As a control, a PBS solution

of Alexa Fluor 488 ( $2 \mu\text{g mL}^{-1}$ ) was used. The concentration of Alexa Fluor 488 was chosen considering a functionalization efficiency of about 10% as calculated by fluorescence spectroscopy (data not shown here). Cells were washed with PBS buffer and fixed in paraformaldehyde (PFA, 4% v/v) for 10 min in the dark. Cells were washed with PBS and the cell membrane was stained by adding Wheat Germ Agglutinin (WGA) Alexa Fluor 555 conjugate ( $2 \mu\text{g mL}^{-1}$ ) for 10 min at  $37^\circ\text{C}$  and washed again. Finally, the cell nuclei were stained with 4',6-diamidino-2-phenylindole (DAPI,  $1 \mu\text{g mL}^{-1}$ ) in PBS solution for 10 min and washed. An inverted confocal fluorescence microscope (ZEISS LSM-700) with appropriate filters was used to evaluate the cellular uptake of the DNPs.

**Statistical Analysis:** Results for continuous variables are presented as means  $\pm$  standard deviation (SD) of at least three independent experiments. Treatment groups were compared with the independent-samples *t* test. qPCR has been repeated a minimum of 3 independent times in triplicate.  $p < 0.05$  was considered statistically significant. All analysis was performed using GraphPad Prism7.

## Supporting Information

Supporting Information is available from the Wiley Online Library or from the author.

## Acknowledgements

S.M. and C.T. contributed equally to this work. The research was funded by: the Italian Association for Cancer Research (AIRC) IG grant no. 21420 "Correlative optical microscopies for cancer imaging" and Italian Ministry for University and Research POR-PLATT to Dr. AC De Luca; My First AIRC Grant (MFAG-2017, #20206) and POR Campania FESR 2014/2020 (Project SATIN) to E.L. M.T. acknowledges financial support from PON-AIM RTDA\_L1 (AIM 1873131-2). The authors also thank Dr. M. Pirozzi of the Euro-Bioimaging facility at the Institute of Biochemistry and Cell Biology (IBBC-CNR) for the TEM analysis, and Dr. M. Marcedula of the Institute of Polymers, Composites and Biomaterials (IPCB-CNR) for FTIR measurements.

## Conflict of Interest

The authors declare no conflict of interest.

## Data Availability Statement

The data that supports the findings of this study are available in the supplementary material of this article.

## Keywords

colorectal cancer cell, drug delivery system, Galunisertib, nanomedicine, SERS-imaging

Received: March 23, 2021

Revised: June 29, 2021

Published online:

[1] S. Vatandoust, T. J. Price, C. S. Karapetis, *World J. Gastroenterol.* **2015**, *21*, 11767.

[2] J. Zugazagoitia, C. Guedes, S. Ponce, I. Ferrer, S. Molina-Pinelo, L. Paz-Ares, *Clin. Ther.* **2016**, *38*, 1551.

- [3] M. R. Papasani, G. Wang, R. A. Hill, *Nanomedicine* **2012**, *8*, 804.
- [4] Y. H. Xie, Y. X. Chen, J. Y. Fang, *Signal Transduction Targeted Ther.* **2020**, *5*, 22.
- [5] D. V. F. Tauriello, A. Calon, E. Lonardo, E. Batlle, *Mol. Oncol.* **2017**, *11*, 97.
- [6] M. A. Nieto, R. Y. Y. J. Huang, R. A. A. Jackson, J. P. P. Thiery, *Cell* **2016**, *166*, 21.
- [7] T. Vu, P. K. Datta, *Cancers (Basel)*. **2017**, *9*, 171.
- [8] A. Calon, E. Lonardo, A. Berenguer-Llargo, E. Espinet, X. Hernando-Momblona, M. Iglesias, M. Sevillano, S. Palomo-Ponce, D. V. F. Tauriello, D. Byrom, C. Cortina, C. Morral, C. Barceló, S. Tosi, A. Riera, C. S. O. Attolini, D. Rossell, E. Sancho, E. Batlle, *Nat. Genet.* **2015**, *47*, 320.
- [9] K. C. Cassidy, I. Gueorguieva, C. Miles, J. Rehm, P. Yi, W. J. Ehlhardt, *Xenobiotica* **2018**, *48*, 382.
- [10] Y. Namiki, T. Fuchigami, N. Tada, R. Kawamura, S. Matsunuma, Y. Kitamoto, M. Nakagawa, *Acc. Chem. Res.* **2011**, *44*, 1080.
- [11] E. Yuba, *J. Mater. Chem. B* **2020**, *8*, 1093.
- [12] D. Arcos, M. Vallet-Regí, *Acta Mater.* **2013**, *61*, 890.
- [13] A. Kumar, X. Zhang, X. J. Liang, *Biotechnol. Adv.* **2013**, *31*, 593.
- [14] C. Schiattarella, R. Moretta, T. Defforge, G. Gautier, B. Della Ventura, M. Terracciano, C. Tortiglione, F. Fardella, P. Maddalena, L. De Stefano, R. Velotta, I. Rea, *J. Biophotonics* **2020**, *13*, 202000272.
- [15] M. Comes Franchini, G. Baldi, D. Bonacchi, D. Gentili, G. Giudetti, A. Lascialfari, M. Corti, P. Marmorato, J. Ponti, E. Micotti, U. Guerrini, L. Sironi, P. Gelosa, C. Ravagli, A. Ricci, *Small* **2010**, *6*, 366.
- [16] T. A. Debele, K. Y. Lee, N. Y. Hsu, Y. T. Chiang, L. Y. Yu, Y. A. Shen, C. L. Lo, *J. Mater. Chem. B* **2017**, *5*, 5870.
- [17] X. Li, G. Salzano, J. Qiu, M. Menard, K. Berg, T. Theodossiou, C. Ladavière, R. Gref, *Front. Bioeng. Biotechnol.* **2020**, *8*, 1.
- [18] C. Schiattarella, M. Terracciano, T. Defforge, G. Gautier, B. Della Ventura, R. Moretta, L. De Stefano, R. Velotta, I. Rea, *Appl. Phys. Lett.* **2019**, *114*, 113701.
- [19] R. Moretta, L. De Stefano, M. Terracciano, I. Rea, *Sensors* **2021**, *21*, 1336.
- [20] I. Rea, N. M. Martucci, L. De Stefano, I. Ruggiero, M. Terracciano, P. Dardano, N. Migliaccio, P. Arcari, R. Taté, I. Rendina, A. Lamberti, *Biochim. Biophys. Acta, Gen. Subj.* **2014**, *1840*, 3393.
- [21] I. Ruggiero, M. Terracciano, N. M. Martucci, L. De Stefano, N. Migliaccio, R. Taté, I. Rendina, P. Arcari, A. Lamberti, I. Rea, *Nanoscale Res. Lett.* **2014**, *9*, 329.
- [22] J. Delasoie, J. Rossier, L. Haeni, B. Rothen-Rutishauser, F. Zobi, *Dalton Trans.* **2018**, *47*, 17221.
- [23] WHO, *IARC Monogr. Eval. Carcinog. Risks to Humans* **1997**, *68*, 306.
- [24] C. Tramontano, G. Chianese, M. Terracciano, L. De Stefano, I. Rea, *Appl. Sci.* **2020**, *10*, 6811.
- [25] M. Terracciano, M. A. Shahbazi, A. Correia, I. Rea, A. Lamberti, L. De Stefano, H. A. Santos, *Nanoscale* **2015**, *7*, 20063.
- [26] I. Rea, M. Terracciano, L. De Stefano, *Adv. Healthcare Mater.* **2017**, *6*, 1601125.
- [27] M. Terracciano, L. De Stefano, C. Tortiglione, A. Tino, I. Rea, *Adv. Biosyst.* **2019**, *3*, 1800247.
- [28] S. Managò, N. Migliaccio, M. Terracciano, M. Napolitano, N. M. Martucci, L. De Stefano, I. Rendina, A. C. De Luca, A. Lamberti, I. Rea, *J. Biophotonics* **2018**, *11*, 201700207.
- [29] M. Terracciano, M. Napolitano, L. De Stefano, A. C. De Luca, I. Rea, *Nanotechnology* **2018**, *29*, 235601.
- [30] G. Gonzalez-Avila, B. Sommer, D. A. Mendoza-Posada, C. Ramos, A. A. Garcia-Hernandez, R. Falfan-Valencia, *Crit. Rev. Oncol. Hematol.* **2019**, *137*, 57.
- [31] Y. Kato, S. Ozawa, C. Miyamoto, Y. Maehata, A. Suzuki, T. Maeda, Y. Baba, *Cancer Cell Int.* **2013**, *13*, 89.
- [32] E. Scarpa, J. L. Bailey, A. A. Janeczek, P. S. Stumpf, A. H. Johnston, R. O. C. Oreffo, Y. L. Woo, Y. C. Cheong, N. D. Evans, T. A. Newman, *Sci. Rep.* **2016**, *6*, 29460.
- [33] M. Pannico, I. Rea, S. Chandrasekaran, P. Musto, N. H. Voelcker, L. De Stefano, *Nanoscale Res. Lett.* **2016**, *11*, 315.
- [34] E. Iglesias, *Molecules* **2020**, *25*, 2890.
- [35] R. M. Bhardwaj, J. A. McMahon, J. Nyman, L. S. Price, S. Konar, I. D. H. Oswald, C. R. Pulham, S. L. Price, S. M. Reutzel-Edens, *J. Am. Chem. Soc.* **2019**, *141*, 13887.
- [36] B. Miranda, R. Moretta, S. De Martino, P. Dardano, I. Rea, C. Forestiere, L. De Stefano, *J. Appl. Phys.* **2021**, *129*, 033101.
- [37] J. F. Mukerabigwi, S. Lei, H. Wang, S. Luo, X. Ma, J. Qin, X. Huang, Y. Cao, *RSC Adv.* **2015**, *5*, 83732.
- [38] K. Khezri, *RSC Adv.* **2016**, *6*, 109286.
- [39] N. Majoul, S. Aouida, B. Bessaïs, *Appl. Surf. Sci.* **2015**, *331*, 388.
- [40] M. Stubbs, P. M. J. McSheehy, J. R. Griffiths, C. L. Bashford, *Mol. Med. Today* **2000**, *6*, 15.
- [41] Z. Ji, H. Liu, L. Yu, Q. Duan, Y. Chen, L. Chen, *Food Hydrocolloids* **2020**, *104*, 105733.
- [42] K. K. Bansal, D. K. Mishra, A. Rosling, J. M. Rosenholm, *Appl. Sci.* **2019**, *10*, 289.
- [43] A. C. De Luca, P. Reader-Harris, M. Mazilu, S. Mariggì, D. Corda, A. Di Falco, *ACS Nano* **2014**, *8*, 2575.
- [44] S. Managò, G. Zito, A. Rogato, M. Casalino, E. Esposito, A. C. De Luca, E. De Tommasi, *ACS Appl. Mater. Interfaces* **2018**, *10*, 12406.
- [45] K. Sivashanmugan, K. Squire, A. Tan, Y. Zhao, J. A. Kraai, G. L. Rorrer, A. X. Wang, *ACS Sens.* **2019**, *4*, 1109.
- [46] J. Fei, L. Wu, Y. Zhang, S. Zong, Z. Wang, Y. Cui, *ACS Sens.* **2017**, *2*, 773.
- [47] J. S. Strukl, J. L. Walter, *Spectrochim. Acta, Part A* **1971**, *27*, 209.
- [48] D. Punihale, R. J. Workman, S. Upadhyay, C. Van Bruggen, A. J. Schmitz, T. M. Reineke, R. R. Frontiera, *J. Phys. Chem. B* **2018**, *122*, 9840.
- [49] F. B. Miguel, J. A. Dantas, S. Amorim, G. F. S. Andrade, L. A. S. Costa, M. R. C. Couri, *Spectrochim. Acta, – Part A* **2016**, *152*, 318.
- [50] B. Fazio, C. D'Andrea, A. Foti, E. Messina, A. Irrera, M. G. Donato, V. Villari, N. Micali, O. M. Maragò, P. G. Gucciardi, *Sci. Rep.* **2016**, *6*, 26952.
- [51] J. A. Efstathiou, D. Liu, J. M. D. Wheeler, H. C. Kim, N. E. Beck, M. Ilyas, A. J. Karayiannakis, N. J. M. C. Mortensen, W. Kmiet, R. J. Playford, M. Pignatelli, W. F. Bodmer, *Proc. Natl. Acad. Sci. USA* **1999**, *96*, 2316.
- [52] A. Maamer-Azzabi, O. Ndozangue-Touriguine, J. Bréard, *Cell Death Dis.* **2013**, *4*, 801.
- [53] S. Colak, P. ten Dijke, *Trends Cancer* **2017**, *3*, 56.
- [54] S. Lamouille, J. Xu, R. Derynck, *Nat. Rev. Mol. Cell Biol.* **2014**, *15*, 178.
- [55] Z. Zhang, S. Zheng, Y. Lin, J. Sun, N. Ding, J. Chen, J. Zhong, L. Shi, M. Xue, *BMC Cancer* **2020**, *20*, 1.
- [56] N. E. Bholra, J. M. Balko, T. C. Dugger, M. G. Kuba, V. Sánchez, M. Sanders, J. Stanford, R. S. Cook, C. L. Arteaga, *J. Clin. Invest.* **2013**, *123*, 1348.
- [57] S. I. Núñez-Olvera, B. Chávez-Munguía, M. C. del Rocío Terrones-Gurrola, L. A. Marchat, J. Puente-Rivera, E. Ruíz-García, A. D. Campos-Parra, C. Vázquez-Calzada, E. R. Lizárraga-Verdugo, R. Ramos-Payán, Y. M. Salinas-Vera, C. López-Camarillo, *Sci. Rep.* **2020**, *10*, 10555.
- [58] H. Zhu, X. Gu, L. Xia, Y. Zhou, H. Bouamar, J. Yang, X. Ding, C. Zwieb, J. Zhang, A. P. Hinck, L. Z. Sun, X. Zhu, *Clin. Cancer Res.* **2018**, *24*, 2780.
- [59] G. Quero, G. Zito, S. Managò, F. Galeotti, M. Pisco, A. De Luca, A. Cusano, *Sensors* **2018**, *18*, 680.